05

Photocatalytic and magnetic properties of zinc ferrite nanoparticles

© K.D. Martinson, A.A. Murashkin

Ioffe Institute,
194064 St. Petersburg, Russia
e-mail: martinsonkirill@mail.ru

Received March 14, 2024
Revised June 15, 2025
Accepted June 15, 2025

zinc ferrite powders with a mean particle size from (5.9 ± 1) to (30.9 ± 3) nm and a crystal phase fraction from 62 % to 99 % were obtained in solution combustion conditions using citric acid as organic fuel with various oxidizer/reducer ratios. It is shown that ferrite formation starts at the oxidizer/reducer ratio of 0.50, while an almost fully X-ray amorphous sample with a mean particle size about 6 nm is formed at 0.25. A solid product containing a single phase — zinc ferrite with a mean particle size of 20−25 nm, is formed in the stoichiometric ratio region of organic fuel. The highest saturation magnetization (43.8 emu/g), residual magnetization (27.2 emu/g) and coercive force (336.2 Oe) were found in a sample synthesized with an oxidizer/reducer ratio of 1.00, which corresponds to the stoichiometric amount of citric acid in the reaction solution. A spectrophotometric survey has shown that all samples facilitated decomposition of an organic dye (rhodamine B). The highest decomposition parameters were recorded in samples containing impurity oxide phases, have the smallest particle size and high percentage of zinc oxide crystal phase.

Keywords: zinc ferrite, solution combustion, citric acid, magnetic properties, photocatalytic properties.

DOI: 10.61011/TP.2025.10.62092.84-24

Introduction

Spinel ferrites have been produced and used in industry over more than 70 years, however, the interest in these materials is steadily growing [1]. In terms of structure, spinel ferrites include compounds corresponding to formula AFe_2O_4, where cation A is a bivalent metal (Mn, Co, Ni, Cu, Zn, etc.). All spinel ferrites feature chemical and thermal stability, and unique set of magnetic and electromagnetic properties, due to which materials of this type are still widely used for a wide range of electronic applications [2]. Spinel ferrites are usually divided into normal spinels where eight tetrahedral positions are occupied by bivalent metal cations, and sixteen octahedral positions are occupied by trivalent iron cations, and inverse spinels that are distinctive in that their sixteen octahedral positions are half-occupied by bivalent metal cations, and the remaining eight octahedral and eight tetrahedral positions are occupied by trivalent iron cations [3]. Zinc ferrite is classified as normal spinel, meaning, in particular, that its inversion degree is equal to zero [4].

Zinc ferrite applications may be divided into classical and new ones that started growing rapidly several decades ago. Classical applications traditionally includes electromagnetic ceramic materials that mainly use multicomponent zinc ferrites, primarily zinc manganese ferrites [5]. Many studies have been published in the field of the effect of dopants (with bivalent transition metal cations used as such) and it has been shown that introduction of manganese into the zinc ferrite lattice considerably improves electromagnetic properties such as permittivity and dielectric loss angle tangent [6]. In terms of classical applications, pure zinc ferrite is of no special interest due to its moderate magnetic and electromagnetic properties. Nevertheless, rapid development of „wet chemistry“ and nanostructure chemistry has resulted in discovery of a lot of new applications for complex oxide systems in general and zinc ferrite in particular [7]. Zinc ferrite nanoparticles are currently widely used as materials for production of sensors and transducers (for example, for gas detection) [8], in magnetic hyperthermia [9], catalysis [10] and photocatalysis [11]. For these applications, streamlined synthesis of nanostructures with controlled particle sizes, morphology and high specific surface areas shall be provided. Therefore, development and investigation of new zinc ferrite nanoparticle production techniques meeting all above-mentioned requirements are a highly topical and essential research problem [12].

To date, there are many known techniques that can be used to produce zinc ferrite nanoparticles for various applications. Traditional solid-phase synthesis using planetary or vibratory mills is still the most common technique [13]. Its popularity is attributable to the fact that it is still the main technique in ferrite material production because of its best scalability [14]. However, despite the ability to produce, in particular, nanoparticles using activator mills, the solid-phase synthesis has a number of significant disadvantages in terms of streamlined synthesis of nanostructures with controlled properties and with respect to producing single-phase objects without impurity oxide phases [15]. Popular techniques for producing complex oxide system nanoparticles, including spinel ferrites, include hydrothermal synthesis [16], sol-gel synthesis [17],

codeposition [18], solution combustion [19], sonochemical synthesis [20], etc. Solution combustion is currently the most promising technique, doesn't require sophisticated expensive equipment and has good prospects for scaling-up [21]. In addition, this technique makes it possible to control many synthesis variables to provide streamlined nanostructure synthesis [22].

There is a large body of literature that is concerned with production of zinc ferrite nanoparticles and investigation of functional properties [1,9,23]. In particular, there is a number of published studies describing zinc ferrite production in solution combustion conditions [4,24,25]. Thus, in [24], $ZnFe_2O_4$ nanoparticles from 19.1 to 113.1 nm in size were produced by solution combustion using urea as organic fuel, and photocatalytic properties were studied in detail on several organic dyes. Disadvantage of the synthesis technique described in [24] is heat treatment in air at temperatures from 400 °C to 1100 °C and the presence of impurity zinc and iron oxide phases when treatment from 400 °C to 600 °C is chosen. Finally, pure zinc ferrite is formed only at a temperature from 700 °C, which negatively affects the mean particle size (larger than 40 nm) and, consequently, photocatalytic properties. Study [25] investigated the influence of various types of organic fuel (glycine, urea and ethylenediaminetetraacetic acid) on structural and magnetic properties of zinc ferrite produced by solution combustion. It has been shown that, depending on the composition of reaction medium, particles with sizes from 10 nm to 27 nm, but with sufficiently small crystal phase fraction and with impurity zinc and iron oxide phases, were produced. Study [4] that used solution combustion and sol-gel synthesis versions with citric acid is the most promising one in terms of producing single-phase samples. The main idea was in synthesizing initial ferrite powder with stoichiometric oxidizer/reducer ratio followed by heat treatment in air at temperatures from 350 °C to 1000 °C. Therefore, all synthesized powders were free of impurity zinc and iron oxides, but the mean particle size was quite large (approximately 50–60 nm).

In this study, zinc oxide nanoparticles were produced by means of solution combustion with citric acid with various f — oxidizer/reducer ratio ($f = 0.25, 0.5, \ldots 1.5$). Although in recent years several studies have been published [4,25] where solution combustion with identical types of organic fuel was used to synthesize zinc ferrite samples, the effect of oxidizer/reducer ratio on structural and functional properties hasn't been studied in detail yet. Nevertheless, by varying the fuel amount smaller particles may be obtained than by varying the heat treatment temperature of combustion products [26].

1. Experimental

The following precursors were used: $Zn(NO_3)_2 \cdot 6H_2O$ (99 %, Neva-reaktiv), $Fe(NO_3)_3 \cdot 9H_2O$ (99 %, Neva-reaktiv), $C_6H_8O_7$ (99 %, Neva-reaktiv), HNO_3 (98 %, Neva-reaktiv) and bidistilled water with resistivity not higher than 5 MΩ·cm. Additional purification of synthesis precursors was not used.

At the first synthesis stage, zinc and iron nitrates were weighed in the amount calculated from the reaction of end product formation, dissolved in 50 ml of distilled water and stirred mechanically during 15 min with addition of several milliliters of 5M nitric acid to prevent formation of complex impurity compounds. After full dissolution of crystalline hydrates, citric acid was added with $f = 0.25$, 0.5, ... 1.5, where $f = 1.00$ is the stoichiometric amount of citric acid calculated from the reaction of formation, and $f = 0.25 - 0.75$ and $f = 1.25 - 1.50$ are reaction solutions with deficiency and surplus of organic fuel, respectively. The solutions thus prepared were stirred again during 15 min and heated using a ceramic stove to almost full water removal from solution and until the self-ignition point was reached to form zinc ferrite with abundant carbon and nitrogen oxide gas release. The end solid product was ground in a ceramic mortar and heat treated in air at 500 °C for 1 h.

The morphology and chemical composition of the synthesized powders were analyzed using energy-dispersive spectroscopy and scanning electron microscopy on the Tescan Vega 3 SBH scanning electron microscope and Oxford INCA accessory. Phase composition analysis and X-ray diffraction analysis were performed by powder X-ray diffractometry using the Rigaku SmartLab 3 diffractometer with $CuK_\alpha 1$ radiation (0.154056 nm) at 40 kV and 30 mA and 2θ from 10 to 80°, at 0.01° intervals and integration time of 3 s. The recorded diffraction patterns were processed in Rigaku SmartLab Studio II, phase composition was determined using ICDD PDF-2 database. Mean crystallite size was calculated using the Scherrer equation:

$$D = \frac{k \cdot \lambda}{\beta \cdot \cos\theta},$$

where k is the crystal shape factor (in isometric approximation was set to 0.94), λ is the X-ray wavelength (CuK_α, $\lambda = 0.15406$ nm), β is the diffraction maximum broadening (in radians), θ is the diffraction maximum position (Bragg angle).

Magnetic parameters of the zinc ferrite samples were analyzed using the Lake Shore 7410 vibration magnetometer at room temperature (298 K) in the field range up to 60,000 Oe with a standard cell. The Shimadzu UV-1800 spectrophotometer was used for spectrophotometric measurements with rhodamine B used as a model dye. For spectrum measurement, 10 mg of initial samples was added to 50 ml of dye solution with a concentration of 25 mg/kg. The solutions thus prepared were stirred for 15 min in total darkness and then irradiated by 18 W deuterium discharge lamp for 50 min. Solutions were sampled at 10 min intervals to measure corresponding spectra.

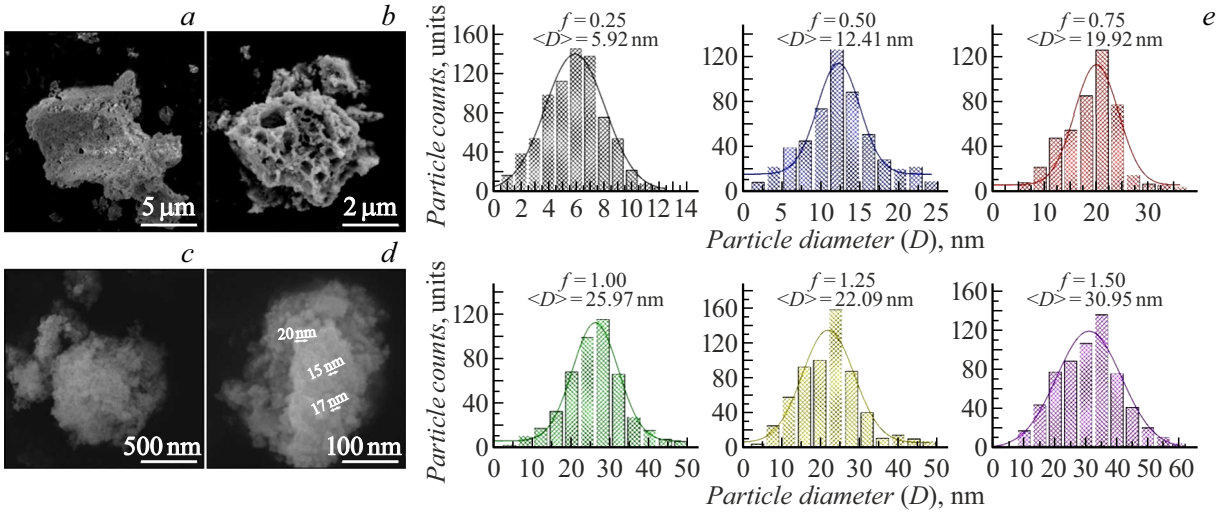

Figure 1. Microphotographs of zinc ferrite synthesized by solution combustion with citric acid at $f = 1.00$ $(a-d)$, histograms of particle size distribution with different f (e).

2. Findings and discussion

2.1. Chemical composition and morphology

Figure 1 shows zinc ferrite powder microphotographs and mean particle size distribution histograms recorded in ImageJ. In terms of morphology, all synthesized compositions represent a typical pattern of solution combustion solid products. This is illustrated by microphotographs with morphology of the $ZnFe_2O_4$ sample synthesized with $f = 1.00$. It can be seen that the sample morphology consists of micron-size agglomerates from 5 to 0.5 μm (Figure 1, $a-c$) that in turn consist of 15–20 nm particles (Figure 1, d). The smallest mean particle size is observed in a sample synthesized with significant deficiency in citric acid ($f = 0.25$) and is equal to 5.92 nm, which is explained by combustion mode and temperature depending on the organic fuel amount. It is known [21,27] that depending the oxidizer/reducer ratio, flame temperature may vary on average from 400 °C to 900 °C, moreover, combustion mode may also vary from glow to overall and surface combustion. As the amount of citric acid in the initial reaction solution increases and, consequently, as the flame temperature increases, particle size grows to 30.95 nm with $f = 1.50$. Thus, the morphology and particle size analysis shows that the produced zinc ferrite particles have a size from 5.92 nm to 30.95 nm and a well-developed morphology typical for complex oxide systems synthesized in solution combustion conditions.

The table demonstrates elemental analysis of all synthesized powders expressed as metals without considering oxygen. The findings demonstrate that experimental chemical composition of all zinc ferrite samples agrees with the design composition within the test method error. The maximum differences are observed in samples synthesized with considerable surplus ($f = 1.25$ and 1.50) and deficiency ($f = 0.25$) of organic fuel and are likely associated with the fact that the zinc ferrite formation process with such ratios takes place incompletely, which was confirmed by the powder X-ray diffractometry data.

Chemical composition of zinc ferrite samples expressed as main components.

Sample, f	Zn, at.%	Fe, at.%
0.25	32.5	67.5
0.50	33.0	67.0
0.75	32.8	67.2
1.00	33.1	66.9
1.25	32.1	67.9
1.50	32.2	67.8

2.2. Phase composition and structural analysis

Phase composition analysis of synthesized compounds has shown that zinc ferrite formation started f equal to 0.50 (Figure 2). With $f = 0.25$, the sample almost totally consists of X-ray amorphous powder with a small inclusion of oxide impurity phases ($> 4\%$). It is known from the literature [28] that formation of zinc ferrite in solution combustion conditions using nitrates as initial components takes place in the temperature range from 370 °C to 450 °C depending on the type of organic fuel. The absence of typical spinel peaks on the diffraction pattern of a sample synthesized with considerable fuel deficiency suggests that the flame temperature with such ratio is lower than the zinc ferrite crystallization temperature. As the oxidizer/reducer ratio increases to 0.50, a sample containing

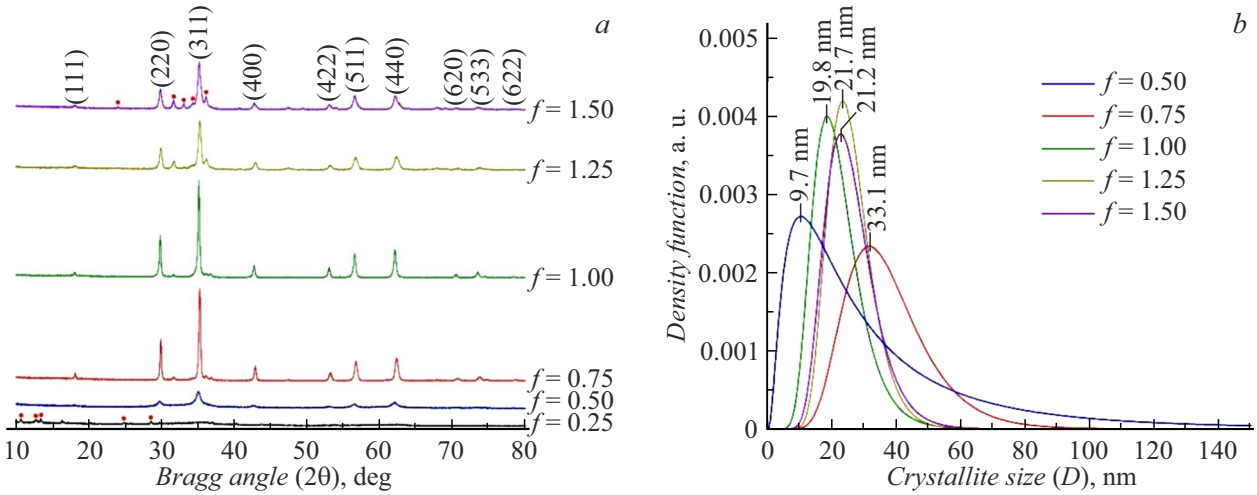

Figure 2. Diffraction patterns (a) and crystallite distribution over the sizes (b) of zinc ferrite nanoparticles synthesized in solution combustion conditions.

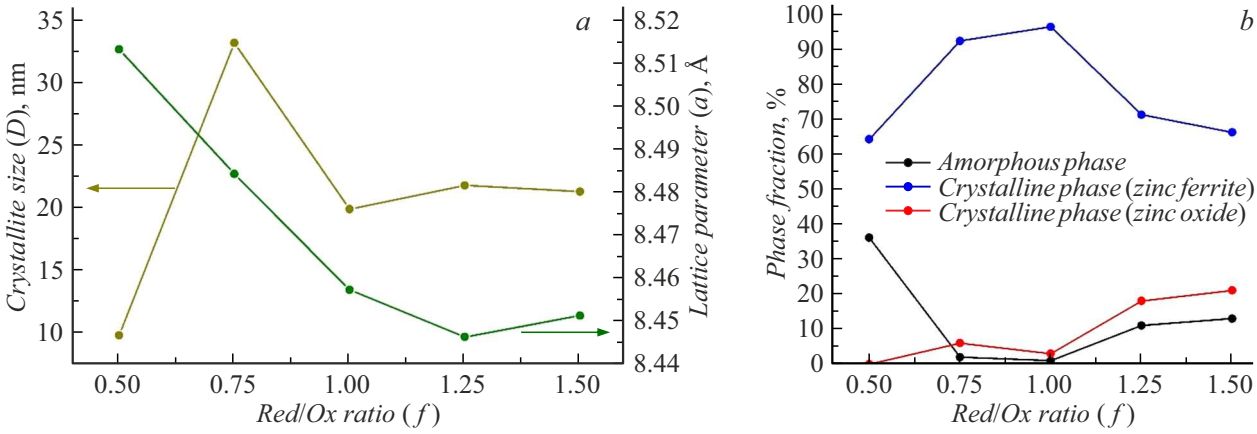

Figure 3. Dependence of structural parameters (a) and relative amount of phases (b) on f.

crystalline and amorphous zinc ferrite phases (JCPDS card # 08-0234 [29]) is formed, no oxide impurity phases were detected. Weighted average crystallite size determined by a fundamental parameter method (Figure 2, b), 9.7 nm, agrees well with particle sizes determined by visual analysis of microphotographs (12.41 nm). As the oxidizer/reducer ratio approaches the stoichiometry point, peak intensity growth is observed for peaks corresponding to the zinc ferrite phase, and peak width is reduced, which indicates the growth of crystal sizes. This also confirms crystallite distribution over sizes, according to which the mean size for samples prepared with $f = 0.75$, 1.00 and 1.25 is equal to 33.1 nm, 19.8 nm and 21.7 nm, respectively. When proceeding to the fuel surplus region, a zinc oxide impurity phase is observed, the fraction of which turns out to be equal to 19 and 22 mass% for samples synthesized at $f = 1.25$ and 1.50, respectively. Occurrence of the zinc oxide phase in these samples is also most likely attributable to the transition from surface to overall combustion and to flame temperature variation.

Dependence of mean crystallite sizes determined using the Scherrer equation, lattice cell parameters and phase compositions on f are shown in Figure 3. The mean crystallite size calculated using the Scherrer equation [19] agrees well with the data obtained using the fundamental parameter method and visual analysis of microphotographs (Figure 1, e). Lattice parameter variations suggest that there is a structural transformation process with $f = 0.50$ and 0.75, which is likely associated with a number of physical and chemical transformations in the amorphous phase consisting of a mixture of uncrystallized ferrite and unreacted precursors as has been previously illustrated by the authors using europium orthoferrite [30]. Variation of phase fraction depending on the chosen fuel/nitrite ratio demonstrates that with $f = 0.50$ a considerable amorphous phase percentage is observed (37 %) and decreases almost to zero in samples synthesized at $f = 0.75$ and 1.00 (i.e. close to the stoichiometry point) and then increases almost to 15 % in samples synthesized with fuel surplus. These data confirm that with $f = 0.50$ the zinc ferrite formation and crystallization process takes place incompletely.

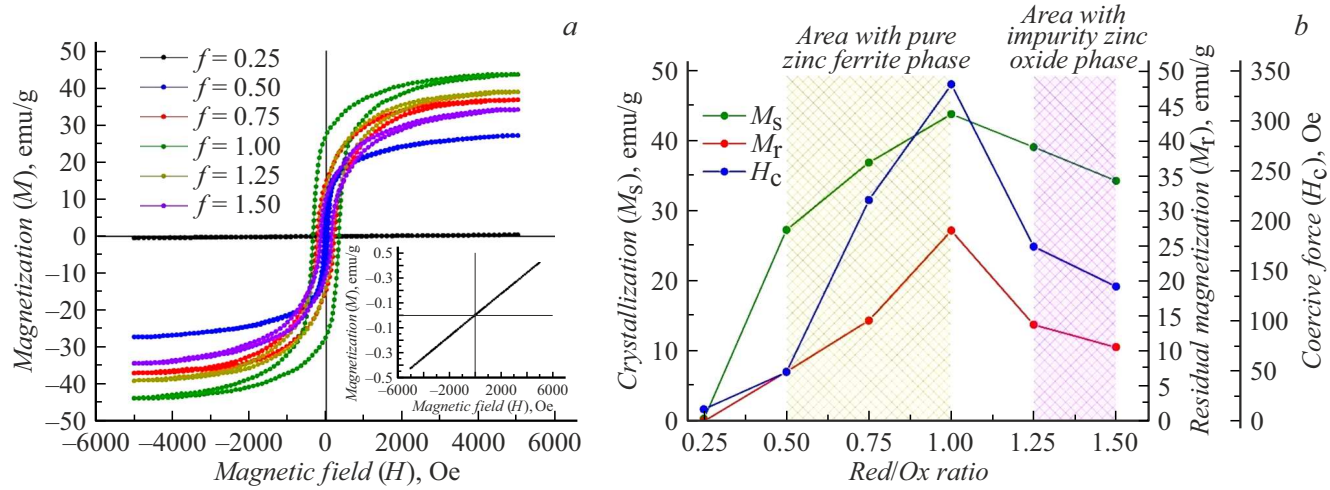

Figure 4. M-H hysteresis loops (a) and dependence of main magnetic parameters (b) on the composition of initial reaction solution.

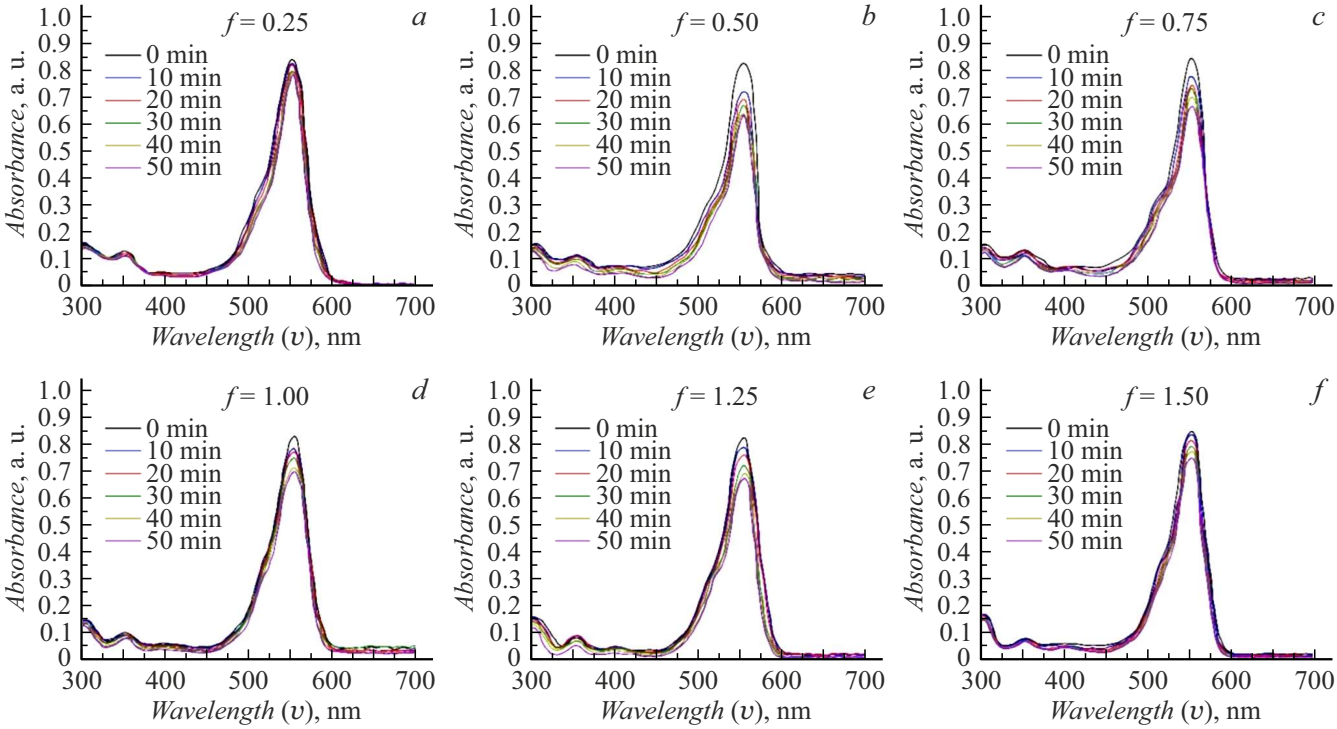

Figure 5. Spectra of rhodamine B photodecomposition depending on zinc ferrite nanoparticle synthesis conditions.

2.3. Magnetic parameters

Features of magnetic behavior of synthesized ferrite nanopowders are defined mainly by the particle size and structural parameters. Figure 4, *a* shows magnetic M-H hysteresis loops of all synthesized samples. A sample synthesized with $f = 0.25$, that has the lowest saturation magnetization, residual magnetization and coercive force, is especially distinguished. In this sample, the process of insertion of Zn^{2+} with magnetic moment between Zn^{2+}-Fe^{2+} sites in the spinel lattice was not fully completed, therefore, there is no magnetic exchange interaction in Zn^{2+}-O-Fe^{2+} sites and no Fe^{3+} transition from Fe^{2+} positions to Zn^{2+} positions as well [31]. This is also confirmed by the powder X-ray diffractometry, from which it follows that a sample with $f = 0.25$ was uncrystallized and is an almost totally amorphous composition with a particle size of approximately 7 nm. As f and, consequently, crystallite size and crystal phase fraction increase, increase in saturation magnetization, residual magnetization and coercive force are observed. Their maximum is reached with $f = 1.00$, where the saturation magnetization is 43.8 emu/g,

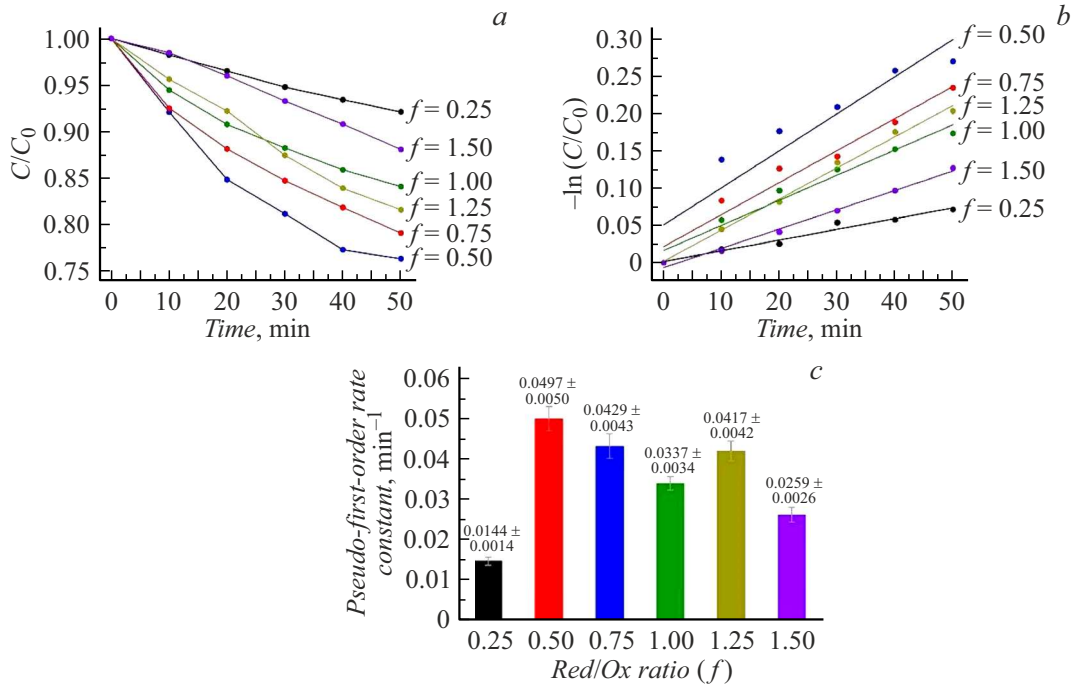

Figure 6. Kinetic curves (a), logarithmic kinetic dependences (b) and rate constants (c) for organic dye (rhodamine B) decomposition reaction in the presence of powders containing nanoscale zinc ferrite particles.

residual magnetization is 27.2 emu/g, and coercive force is 336.2 Oe (Figure 4, b). As f increases towards fuel surplus in the reaction solution, decrease in the main magnetic parameters is observed, which is primarily attributable to the increase in the amorphous phase fraction (~ 20 mass%) and occurrence of the impurity zinc oxide phase.

2.4. Photocatalytic characterization

Figure 5 shows absorbance spectra of solution containing Rhodamine B organic dye, after the photodegradation process in the presence of synthesized zinc ferrite powders. The findings have shown that the particle sizes and structural parameters of the synthesized samples had a significant effect on the photodegradation efficiency. Thus, notwithstanding that the smallest particle size corresponds to the sample obtained with $f = 0.25$, significant reduction of the absorbance signal in the dye solution was not observed at 554 nm (which corresponds to the Rhodamine B absorbance maximum). This feature of photocatalytic behavior is also associated with the phase composition of this sample and the absence of a crystalline spinel ferrite phase. According to the provided data, the most significant reduction of absorbance peak intensity in zinc ferrite samples synthesized at $f = 0.50$, 0.75 and 1.00 was recorded in the initial treatment period (10 min), whilst samples synthesized with other ratios demonstrated smoother intensity reduction throughout the observation period. This is attributable to the features of phase composition of samples synthesized with the oxidizer/reducer ratio of 1.25 and 1.50, that contain both a significant amorphous phase percentage and the zinc oxide phase. The highest dye decomposition percentage (76.7 %) was recorded for a sample synthesized at $f = 0.50$, which is explained by a small particle size (12.4 nm) and the presence of one zinc ferrite phase. The obtained dependences (Figure 6) generally show that the particle size (and, consequently, specific surface area of the samples) and phase composition are the key factors that affect photocatalytic activity. Calculation of the rate constant (Figure 6, b) has shown that the highest rate constants are reached for samples synthesized at $f = 0.5$ (0.0497 ± 0.0050) and 0.75 (0.0429 ± 0.0043), and the lowest rate constants are observed for a sample synthesized at $f = 0.25$ (0.0144 ± 0.0014). The obtained data agree well with the mean crystallite size and crystalline and amorphous phase fraction data. From this standpoint, samples synthesized in the oxidizer/reducer ratio range from 0.50 to 0.75 look as the most promising because they combine one crystalline zinc ferrite phase, the absence of impurity zinc and iron oxide phases, and small particle size.

Conclusion

To identify the effect of the oxidizer/reducer ratio on the morphology, structure, magnetic and photocatalytic properties, zinc ferrite nanopowders were synthesized in this study using the solution combustion technique with citric acid as organic fuel. It has been shown that, depending on the chosen oxidizer/reducer ratio f, the mean zinc ferrite particle size varied from 5.9 nm to 30.9 nm. In addition,

it has been found that with $f = 0.50$, 0.75 and 1.00 a zinc ferrite sample containing two phases (amorphous and crystalline zinc ferrite phases) was formed, whilst with ratios of 1.25 and 1.50 appearance of the impurity zinc oxide phase is observed. Investigation of magnetic properties has demonstrated that particles with saturation magnetization, residual magnetization and coercive force in the ranges from 0.43 to 43.8 emu/g, from 0.05 to 27.2 emu/g and from 12.3 to 336.2 Oe, respectively, could be obtained depending on the synthesis conditions. Analysis of photocatalytic activity of the synthesized powders made it possible to determine the dependence of the degree of organic dye decomposition on the particle size and degree of crystallinity.

Acknowledgments

The authors would like to express their gratitude to the Engineering Center of the St. Petersburg State Institute of Technology (Technological University) for their assistance in the study of morphology and structure.

Conflict of interest

The authors declare no conflict of interest.

References

[1] S.N. Pund, P.A. Nagawade, A.V. Nagawade, S.R. Thopate, A.V. Bagade. Materials Today: Proceed., **60** (3), 2194 (2022). DOI: 10.1016/j.matpr.2022.02.444
[2] M. Sugimoto. J. American Ceramic Society, **82** (2), 269 (1999). DOI: 10.1111/j.1551-2916.1999.tb20058.x
[3] J.B. Franklin, G.T. Anand, G.M. Sujitha, S.J. Sundaram, A.D. Raj, K. Kaviyarasu. Mater. Today: Proceed., **68** (3), 593 (2022). DOI: 10.1016/j.matpr.2022.08.429
[4] J.K. Jogi, S.K. Singhal, R. Jangir, A. Dwivedi, A.R. Tanna, R. Singh, M. Gupta, P.R. Sagdeo. J. Electron. Mater., **51**, 5482 (2022). DOI: 10.1007/s11664-022-09813-2
[5] M. Kacki, M.S. Rylko, J.G. Hayes, C.R. Sullivan. IEEE Transactions on Power Electronics, **37** (12), 15152 (2022). DOI: 10.1109/TPEL.2022.3189671
[6] P. Pengdei, Z. Ning. J. Magn. Magn. Mater., **416**, 256 (2016). DOI: 10.1016/j.jmmm.2016.05.018
[7] S.J. Salih, W.M. Mahmood. Heliyon, **9** (6), E16601 (2023). DOI: 10.1016/j.heliyon.2023.e16601
[8] K. Wu, J. Li, C. Zhang. Ceramics Intern., **45** (9), 11143 (2019). DOI: 10.1016/j.ceramint.2019.03.086
[9] P. Sahoo, P. Choudhary, S.S. Laha, A. Dixit, O.T. Mefford. Chem. Commun., **81** (59), 12065 (2023). DOI: 10.1039/D3CC01637D
[10] N. Maji, H.S. Dosanjh. Magnetochemistry, **9** (6), 156 (2023). DOI: 10.3390/magnetochemistry9060156
[11] A. Arimi, L. Megatif, L.I. Granone, R. Dillert, D.W. Bahnemann. J. Photochem. Photobiology A: Chem., **366**, 118 (2018). DOI: 10.1016/j.jphotochem.2018.03.014
[12] S. Malik, K. Muhammad, Y. Waheed. Molecules, **28** (2), 661 (2023). DOI: 10.3390/molecules28020661
[13] G. Stefanic, S. Krehula, I. Stefanic. Dalton Transactions, **44** (43), 18870 (2015). DOI: 10.1039/C5DT02498F
[14] K.D. Martinson, I.B. Panteleev, K.A. Steshenko, V.I. Popkov. J. European Ceramic Society, **42**, 4363 (2022). DOI: 10.1016/j.jeurceramsoc.2022.02.059
[15] S.K. Dutta, M. Akhter, J. Ahmed, M.K. Amin, P.K. Dhar. Biointerface Research Appl. Chemi., **12** (4), 4399 (2022). DOI: 10.33263/BRIAC124.43994416
[16] G.M. Alzoubi. J. Superconductivity Novel Magnetism, **35**, 2417 (2022). DOI: 10.1007/s10948-022-06230-8
[17] F. Iqbal, M.I.A. Mutalib, M.S. Shaharun, M. Khan, B. Abdullah. Procedia Engineer., **148**, 787 (2016). DOI: j.proeng.2016.06.563
[18] Y.B. Kannan, R. Saravanan, N. Srinivasan, K. Praveena, K. Sadhana. J. Mater. Sci.: Mater. Electron., **27**, 12000 (2016). DOI: 10.1007/s10854-016-5347-y
[19] K.D. Martinson, I.A. Cherepkova, V.V. Sokolov. Glass Phys. Chem., **44**, 21 (2018). DOI: 10.1134/S1087659618010091
[20] P.P. Goswami, H.A. Choudhury, S. Chakma, V.S. Moholkar. Industrial Engineering Chem. Research, **52** (50), 17848 (2013). DOI: 10.1021/ie401919x
[21] A. Varma, A.S. Mukasyan, A.S. Rogachev, K.V. Manukyan. Chem. Rev., **116** (23), 14493 (2016). DOI: 10.1021/acs.chemrev.6b00279
[22] E. Novitskaya, J.P. Kelly, S. Bhaduri, O.A. Graeve. Intern. Mater. Rev., **66** (3), 188 (2021). DOI: 10.1080/09506608.2020.1765603
[23] M. Ochmann, V. Vrba, J. Kopp, T. Ingr, O. Malina, L. Machala. Nanomaterials, **12** (17), 2987 (2022). DOI: 10.3390/nano12172987
[24] T.P. Oliveira, G.N. Marques, M.A.M. Castro, R.C.V. Costa, J.H.G. Rangel, S.F. Rodrigues, C.C. Santos, M.M. Oliveira. J. Mater. Res. Technol., **9** (6), 15001 (2020). DOI: 10.1016/j.jmrt.2020.10.080
[25] F. Riyanti, W. Purwaningrum, N. Yuliasari, S. Putri, N. Aprianti, P.L. Harianti. Turkish J. Chem., **46**, 1875 (2022). DOI: 10.55730/1300-0527.3487
[26] S.V. Dyachenko, K.D. Martinson, I.A. Cherepkova, A.I. Zhernovoi. Russ. J. Appl. Chem., **89**, 535 (2016). DOI: 10.1134/S1070427216040029
[27] K.D. Martinson, I.S. Kondrashkova, M.I. Chebanenko, A.S. Kiselev, T.Yu. Kiseleva, V.I. Popkov. J. Rare Earths, **40** (2), 296 (2022). DOI: 10.1016/j.jre.2021.01.001
[28] R.M. Borade, S.B. Somvanshi, S.B. Kale, R.P. Pawar, K.M. Jadhav. Mater. Res. Express, **7**, 016116 (2020). DOI: 10.1088/2053-1591/ab6c9c
[29] D.A. Vieira, V.C.S. Diniz, D.R. Cornejo, A.C.F.M. Costa, R.H.G.A. Kiminami. Mater. Sci. Forum, **775**, 415 (2014). DOI: 10.4028/www.scientific.net/MSF.775-776.415
[30] V.I. Popkov, K.D. Martinson, I.S. Kondrashkova, M.O. Enikeeva, V.N. Nevedomskiy, V.V. Panchuk, V.G. Semenov, M.P. Volkov, I.V. Pleshakov. J. Alloys and Compounds, **859**, 157812 (2021). DOI: 10.1016/j.jallcom.2020.157812
[31] S.O. Aisida, I. Ahmad, T.-K. Zhao, M. Maaza, F.I. Ezema. J. Macromolecular Sci., Part B, **59** (5), 295 (2020). DOI: 10.1080/00222348.2020.1713519

Translated by E.Ilinskaya